remote sensing

MDPI

Article

Integrating Remote-Sensing and Assimilation Data to Improve Air Temperature on Hot Weather in East China

Suosuo Li [1], Yuanpu Liu [2,*], Yongjie Pan [1], Zhe Li [1] and Shihua Lyu [3]

[1] Key Laboratory of Land Surface Process and Climate Change in Cold and Arid Regions, Northwest Institute of Eco-Environment and Resources, Chinese Academy of Sciences, Lanzhou 730000, China; liss@lzb.ac.cn (S.L.); panyongjie@lzb.ac.cn (Y.P.); lizheatm@lzb.ac.cn (Z.L.)
[2] Key Laboratory of Arid Climatic Change and Reduction Disaster of Gansu Province, Institute of Arid Meteorology, China Meteorological Administration, Lanzhou 730020, China
[3] Plateau Atmosphere and Environment Key Laboratory of Sichuan Province, School of Atmospheric Sciences, Chengdu University of Information Technology, Chengdu 610225, China; slu@cuit.edu.cn
* Correspondence: lyp@lzb.ac.cn

Abstract: Land-surface characteristics (LSCs) and land-soil moisture conditions can modulate energy partition at the land surface, impact near-surface atmosphere conditions, and further affect land–atmosphere interactions. This study investigates the effect of land-surface-characteristic parameters (LSCPs) including albedo, leaf-area index (LAI), and soil moisture (SM) on hot weather by in East China using the numerical model. Simulations using the Weather Research and Forecasting (WRF) Model were conducted for a hot weather event with a high spatial resolution of 1 km in domain 3 by using ERA-Interim forcing fields on 20 July 2017 until 16:00 UTC on 25 July 2017. The satellite-based albedo and LAI, and assimilation-based soil-moisture data of high temporal–spatial resolution, which are more accurate to match fine weather forecasts and high-resolution simulations, were used to update the default LSCPs. A control simulation with the default LSCPs (WRF_CTL), a main sensitivity simulation with the updated LSCP albedo, LAI and SM (WRF_CHAR), and a series of other sensitivity simulations with one or two updated LSCPs were performed. Results show that WRF_CTL could reproduce the spatial distribution of hot weather, but overestimated air temperature (Ta) and maximal air temperature (Tamax) with a warming bias of 1.05 and 1.32 °C, respectively. However, the WRF_CHAR simulation reduced the warming bias, and improved the simulated Ta and Tamax with reducing relative biases of 33.08% and 29.24%, respectively. Compared to the WRF_CTL, WRF_CHAR presented a negative sensible heat-flux difference, positive latent heat flux, and net radiation difference of the area average. LSCPs modulated the partition of available land-surface energy and then changed the air temperature. On the basis of statistical-correlation analysis, the soil moisture of the top 10 cm is the main factor to improve warming bias on hot weather in East China.

Keywords: land-surface characteristics; hot weather; air temperature; WRF model; East China

check for updates

Citation: Li, S.; Liu, Y.; Pan, Y.; Li, Z.; Lyu, S. Integrating Remote-Sensing and Assimilation Data to Improve Air Temperature on Hot Weather in East China. *Remote Sens.* **2021**, *13*, 3409. https://doi.org/10.3390/rs13173409

Academic Editor: Itamar Lensky

Received: 24 June 2021
Accepted: 24 August 2021
Published: 27 August 2021

Publisher's Note: MDPI stays neutral with regard to jurisdictional claims in published maps and institutional affiliations.

Copyright: © 2021 by the authors. Licensee MDPI, Basel, Switzerland. This article is an open access article distributed under the terms and conditions of the Creative Commons Attribution (CC BY) license (https://creativecommons.org/licenses/by/4.0/).

1. Introduction

With global warming, the intensity and frequency of hot weather are generally rising [1]. China often suffers from hot weather, East China (EC), where the summer mean air temperature (Ta) is over 27.4 °C [2,3]. Since the 1990s, the intensity of hot weather has significantly increased in EC [2,3], affecting human health and life, energy supply and demand, water resources, and agricultural production, and causing economic losses [4]. Many studies showed that the increase in high temperature is closely related to land-surface heterogeneity [5]. The EC region has experienced rapid urbanization with economic and social development, which resulted in diverse and complex land-surface characteristics (LSCs) [6,7]. Studies found that some hot weather is sensitive to near-surface conditions and LSCs [4,8,9]. Therefore, the impact of LSC is becoming increasingly important for understanding hot weather in EC [10].

The land surface has long been recognized as second in importance only to ocean-surface temperature as a driver of climate [11,12]. LSCs, which are a crucial part of the land-surface model and the basic forcing parameters of land-surface boundary conditions [13], can affect the distribution of land-surface energy fluxes and local or regional mesoscale circulation [10,14]. A better description of land-surface characteristic parameters (LSCPs) can improve regional land simulation, and even improve land–atmosphere interactions [13,15–18]. Previous studies showed that, by using satellite-based land cover/use, green-vegetation fraction, leaf-area index (LAI), and albedo, simulated results are significantly improved [18–20]. The MODIS-NDVI-based green vegetation fraction can reflect the realistic increase in vegetation cover, more accurately present seasonal variation in China, obviously improve the 2 m air temperature, and effectively increase the correlation coefficient between simulations and observations [21]. Replacing the default value of WRF by using the satellite-based green-vegetation fraction and albedo can result in the largest improvement of nocturnal air temperature, and reduce root-mean-square deviation [5]. Integrating MODIS land use, LAI, green vegetation fraction, and albedo dramatically improved the performance of WRF [22].

Meanwhile, SM, as a critical component of land surface [4], plays an important role in numerical models [23], which can significantly influence the heat and water exchanges between atmosphere and land surface through evapotranspiration [23]. On the basis of past modeling and observational studies, researchers concluded that the SM could significantly impact temperature and precipitation when soil-moisture–atmosphere interactions are strong [24–27]. On the basis of the global land–atmosphere coupling experiment, Koster et al. (2006) [28] identified EC as a strong soil moisture–temperature coupling region [24]. Observational studies showed that SM influences temperature in EC, and previously drier surface conditions might intensify hot summer extremes [24,25]. Various numerical model studies indicated that SM significantly impacts temperature over East Asia [24,27,29], and the studies highlighted the critical role of SM for daily mean and maximal temperature [4,30]; under low SM conditions, the hot weather can be amplified [9]. Proper SM is crucial to performing hydrometeorological processes for numerical simulations, especially for short-term simulations [24,31].

Another issue related to numerical simulations is high-resolution simulations (with grid spaces of a few km), which are required both for understanding regional weather and climate, and for hydrological and ecosystem studies [32,33]; this can produce good results and reduce errors [33]. Many studies showed that increasing the spatial resolution of numerical models can effectively improve simulation accuracy and obtain better results [33–36]. Increasing the spatial resolution of models can effectively improve simulation accuracy by resolving small-scale physical processes [33]. Nevertheless, high-resolution simulations need more refined and accurate LSCPs to be matched.

Regional numerical models require prescribed boundary conditions, such as land use, LAI, albedo, vegetation height and zero plane displacement height, and green-vegetation fraction. In the WRF model, whether traditionally looking up tables dependent on vegetation type or using climatology-satellite-based surface characteristics, it is difficult to match fine weather forecasts or high-resolution simulations. Near-real-time satellite-based LSCPs and assimilation-based SM data are used in regional numerical models, which greatly improve model performance [8,10,13,37,38]. At Earth's surface, vegetation-related parameters including LAI, land surface albedo, and SM control the partitioning of energy fluxes and water-vapor transport; thus, land-surface conditions in some regions yield more significant feedback influence [39].

In the present study, using the method of fine weather forecast and high-resolution simulation to investigate the impact of LSCPs on hot weather in EC, the land-surface condition near-real-time satellite-based MODIS albedo and LAI data, and assimilation-based SM data were integrated into the WRF model to improve the air-temperature simulation on hot weather in EC. Then, the mechanism of the impact of LSC on hot weather was researched by analyzing the energy fluxes.

2. Synoptic Weather Conditions, Data, and Model Setup

2.1. Background

EC is located in the East Asian monsoon area (Figure 1), which is the main area of China's economic development. With economic and social development, the EC region presents a more diverse and complex LSC than before [6,7]. At the same time, extreme weather events, including hot weather, heavy rain, hail and cyclones frequently occur in EC.

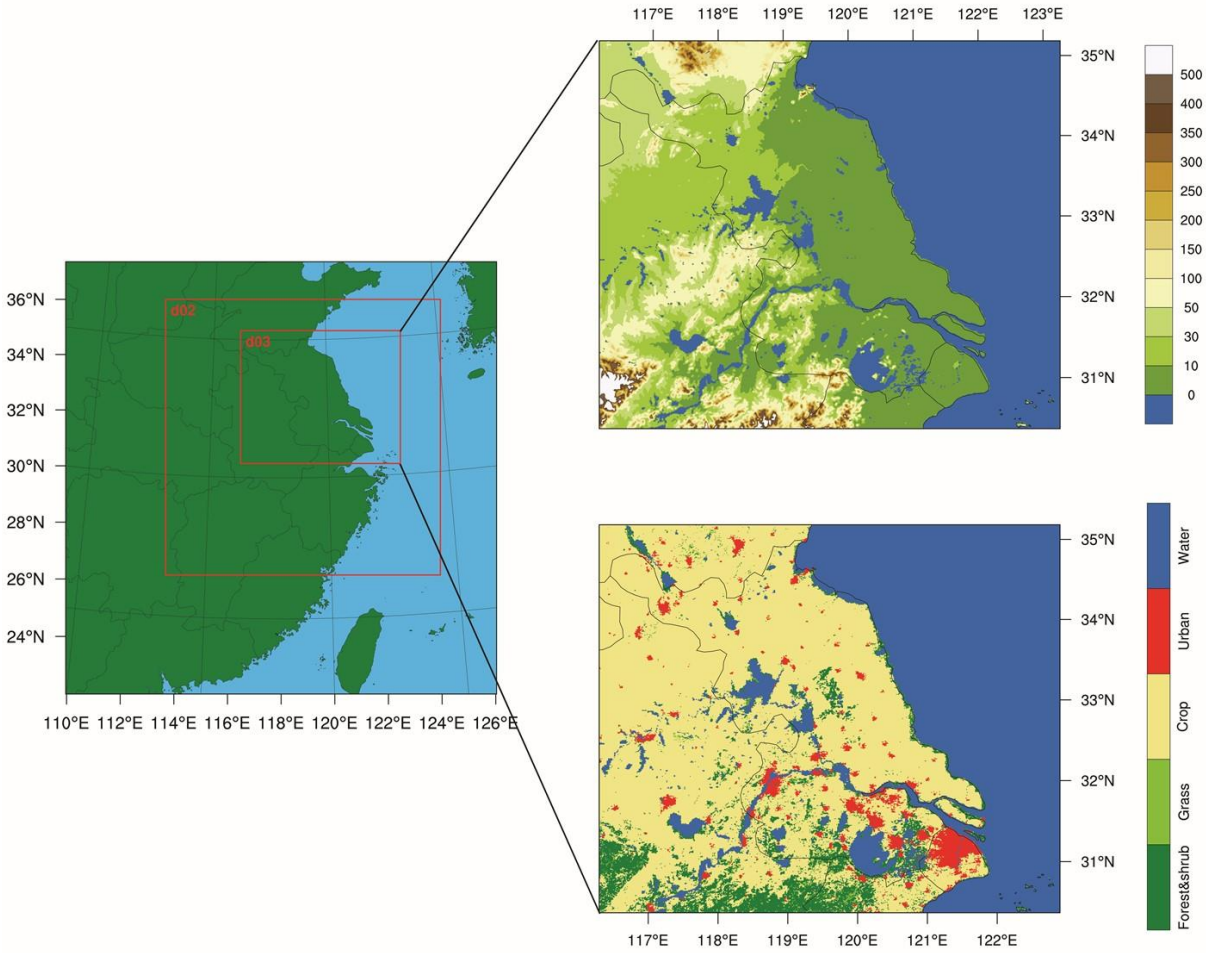


Figure 1. Three nested WRF modeling domains used for numerical simulation, topography height (unit: m), and the main land-use categories in the third domain.

In recent years, due to global warming, high-temperature and heatwave weather occurs frequently during summer in China, and a wide range of record-breaking high temperatures appeared one after another [40], and 2017 was the warmest year on record without an El Niño affecting it; the hot weather showed obvious features of high intensity, long duration, and large area [40]. In late July 2017, the averaged maximal air temperature was more than 4 °C than that of the historical period, the number of high-temperature days was 3 to 6 days more than that of the historical period, and some stations broke the station's historical records [40]. In 21–25 July 2017, 500 hPa, the Asian middle and high latitudes had a trough and a ridge. The ridge was located in northern Siberia, and the trough was located in the northern part of Japan. The center of the subtropical high was located northward, and the southernmost part of China was controlled by the subtropical ridge (Figure 2). Strong downdrafts and anticyclonic circulations stabilized the atmosphere and eventually led to hot weather [40].

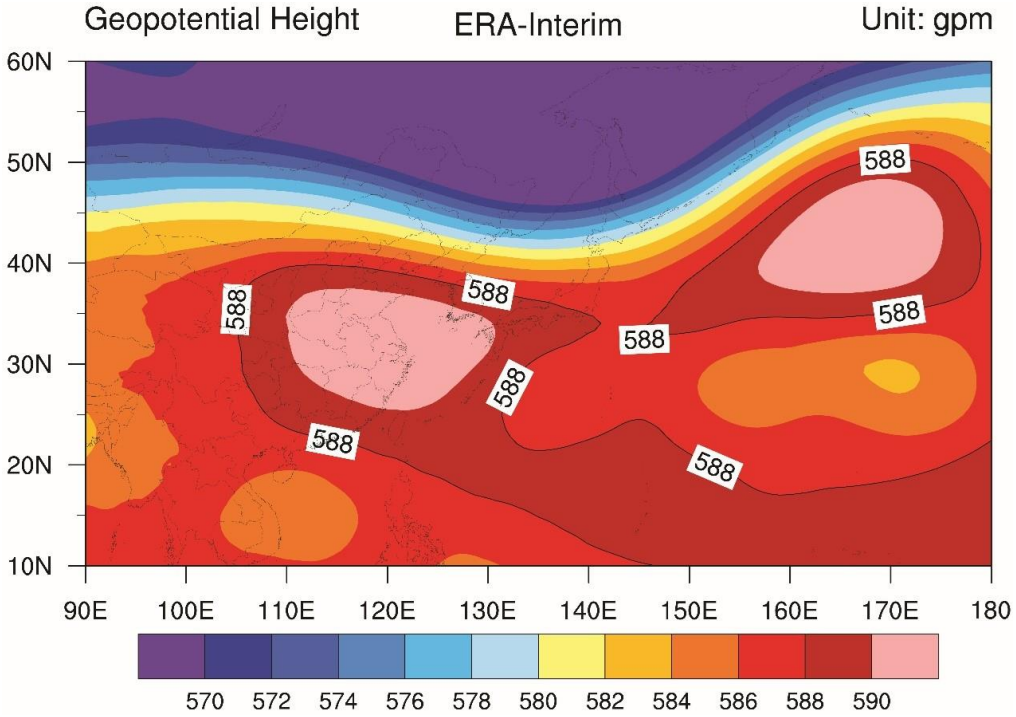


Figure 2. Synoptic weather pattern from ERA-Interim reanalysis data showing geopotential height (unit: gpm) at 500 hPa for the period from 21 to 25 July 2017 around East China.

2.2. Data

In the WRF model, default LAI and albedo data are derived from MODIS and AVHRR, respectively, which are better, and can show spatial distribution and temporal change characteristics of 12 months comparing traditional parameter tables depending on vegetation type [13,20,41,42]. However, the default LAI and albedo with coarser spatiotemporal features and without interannual variation do not display realistic conditions. In this study, the albedo for updating the lower boundary condition of WRF was derived from MODIS Collection 6 land products based on Terra and Aqua, with a 1 day temporal resolution and about 1 km horizontal resolution [43,44]. The LAI for updating the lower boundary condition of WRF was also derived from MODIS Collection 6 land products based on Terra and Aqua, with a 4 day temporal resolution and about 500 m horizontal resolution [43,44].

In addition, the SM is an important initial condition for the RCM. Initial SM data are obtained from forcing data, and those are often reanalysis data of global circulation models [24,31]. For example, in the WRF model, initial SM fields can be supplied from GFS, FNL, NCEP, ECMWF ERA-Interim, or JRA55 and other similar general atmospheric circulation models or general atmosphere–ocean circulation models, which, however, have coarse resolution [24,31]. Inadequate resolution is the main problem with this type of soil-moisture initialization [31]. For example, ERA-Interim (ERA) reanalysis data have a resolution of 0.75° × 0.75°, which is higher than that of similar reanalysis data, that is to say, one grid covers about 90 × 90 km in the middle latitude. In our study, the smallest domain, Dh-3, had a 1 km resolution, which means that one value in the ERA data represented a value of 90 × 90 grids, thus lacking realistic representation and spatial variations [31]. The China Meteorological Administration (CMA) Land Data Assimilation System (CLDAS) SM fields were used to update the initial SM in this work, with a high spatial resolution of 0.0625° × 0.0625°, and a high temporal resolution of 1 day. CLDAS SM and the station observation SM matched very well, had a region average correlation coefficient of 0.89, root-mean-square error of 0.02 m^3m^{-3}, and a bias of 0.01 m^3m^{-3}, and CLDAS SM was better than similar assimilation SM data of other agencies (http://data.cma.cn/dataService/cdcindex/datacode/NAFP_CLDAS2.0_RT.html, accessed on

11 February 2020). Therefore, satellite-based MODIS albedo data and LAI data, and assimilation-based CLDAS SM data were relatively reliable to update the LSCPs in the WRF model in EC (Table 1).

Table 1. Comparisons of LAI and albedo between WRF climatology and MODIS-derived datasets.

	WRF_CTL	WRF_CHAR
Albedo	AVHRR climatological monthly albedo with 0.5° resolution	MODIS Collection 6 daily albedo with 1 km resolution
LAI	MODIS climatological monthly LAI with 0.5° resolution	MODIS Collection 6 4 day LAI with 500 m resolution
Soil moisture	ERA_Interim reanalysis data with 0.75° resolution	CLDAS daily assimilation data with 0.0625° resolution

Automatic hourly surface weather observation stations of 2 m air temperature datasets, which are produced and can be downloaded on the Climatic Data Center, the National Meteorological Information Center, CMA (http://data.cma.cn/site/index.html, accessed on 11 February 2020), were used to assess the simulated air temperature (Ta) and maximal air temperature (Tamax).

2.3. Model Setup

The WRF model, which was developed by NCAR/NCEP, the Forecast Systems Laboratory, and other university scientists, is widely used in weather forecast or prediction and long-term research [20,45,46]. The WRF model is also widely used to research extreme weather, especially during heatwaves or hot weather [9,47–50].

In this study, we used WRF model version 3.8.1 to research hot weather by using physical schemes and parameterizations as follows: WSM6 microphysics scheme, RRTM longwave radiation scheme, Dudhia shortwave radiation scheme, MM5 Monin–Obukhov surface-layer scheme, Bougeault and Lacarrere TKE boundary-layer scheme, and the unified Noah land-surface model. Three nested domains with 25, 5, and 1 km horizontal resolution were used in the simulation, respectively (Figure 2). The innermost domain-3 covered most of the area of the Yangtze River Delta, including Jiangsu province, Shanghai city, and most of Anhui province, which covered the most area of EC. Topographical height is relatively flat, and most of the area of topography height was lower than 100 m in the studied area (Figure 2). Crop is the main land-use type except sea, followed forest, shrub, water (lakes and rivers), urban, and grass covering small areas (Figure 2). All simulations used the ERA-Interim (ERA) 6 h boundary conditions. Simulations were initialized at 00:00 UTC (0800 LST) on 20 July 2017 until 16:00 UTC 25 July 2017 (0000 LST), and the last 5 days of LST were analyzed.

We first performed two simulations. First, the control simulation (WRF_CTL) in which the default LSCP albedo and LAI were used and the SM data initialized by forcing fields ERA (data details described in Section 2.2). Second, the sensitivity simulation in which the LSCP albedo, LAI, and four layers of SM for initialization were updated on the basis of MODIS albedo and LAI and CLDAS SM (WRF_CHAR; data details described in Section 2.2). In addition, a series of supplied sensitivity simulations were performed, which included the ALB simulation (updated the albedo on the basis of the MODIS albedo), LAI simulation (updated the LAI on the basis of MODIS LAI), ALL simulation (updated the albedo and LAI on the basis of MODIS albedo and LAI), and CLDAS simulation (updated the SM on the basis of CLDAS SM). For LSC data processing, if the MODIS albedo was missing, the nearest years' valid value was used. Then, the albedo, LAI, and CLDAS SM datasets were reprojected onto the WRF Lambert projection to coincide with the WRF model. All data were interpolated to 6 h intervals LSCPs to match with our WRF model's setups inputs by using a simple linear method.

3. Results

3.1. LSCP Comparison

For the LSC, the WRF default albedo showed very coarse spatial distribution characteristics. It mainly displayed values of 0.14–0.16 in most research areas, and there were some variations south and east of Jiangsu province, and north of Anhui province (Figure 3(a1)). The MODIS albedo had more accurate spatial distribution characteristics and wide-ranging variations of 0.06–0.24, and the albedo was higher in the northwestern study area than that in the southeastern area (Figure 3(a2,a3)). The area-averaged MODIS albedo was higher by 0.005 (3.40%) than the default albedo. The LAI showed a similar spatial distribution difference with that of the land-surface albedo. Besides accuracy spatial distribution characteristics (Figure 3(b1,b2)), the MODIS LAI was higher by 1.5–3.0 m^2m^{-2} in the southwestern study area and lower by -0.5 to -1.5 m^2m^{-2} in the northeastern study area (Figure 3(b3)). The area average MODIS LAI was 2.79 m^2m^{-2}, which was higher by 11.15% than the default LAI of 2.51 m^2m^{-2}.

The ERA SM and the CLDAS SM had different spatial distributions in the four soil layers. The ERA SM displayed higher values of 0.25–0.3 m^3m^{-3} in the western study area and lower values of 0.15–0.25 m^3m^{-3} in four layers; in contrast, the CLDAS SM presented higher values of 0.25–0.35 m^3m^{-3} in the southern study area (Figure 3(c1,c2,d1,d2)). The figures of SM differences showed that there were negative differences of -0.01 to -0.03 m^3m^{-3} in the western middle study area, and positive differences of 0.01–0.15 m^3m^{-3} in four soil layers (Figure 3(c3,d3)); the area-averaged differences were 0.032, 0.043, 0.045, and 0.053 m^3m^{-3}, respectively, and the relative differences were 12.36%, 15.87%, 15.77%, and 18.09%, respectively in the four soil layers, which gradually increased with the change in soil depth (SM figures of 60 and 100 cm are not shown).

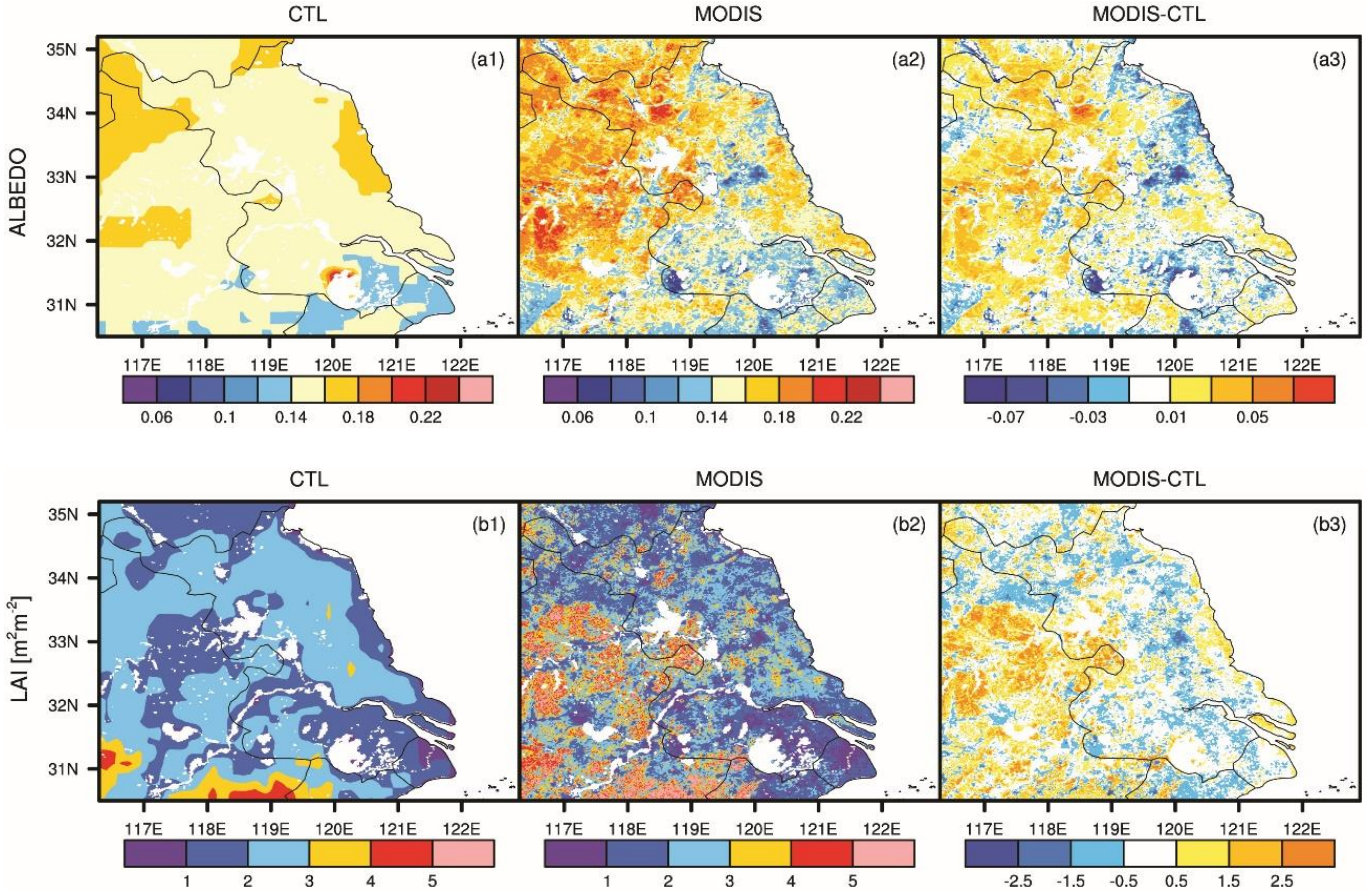


Figure 3. *Cont.*

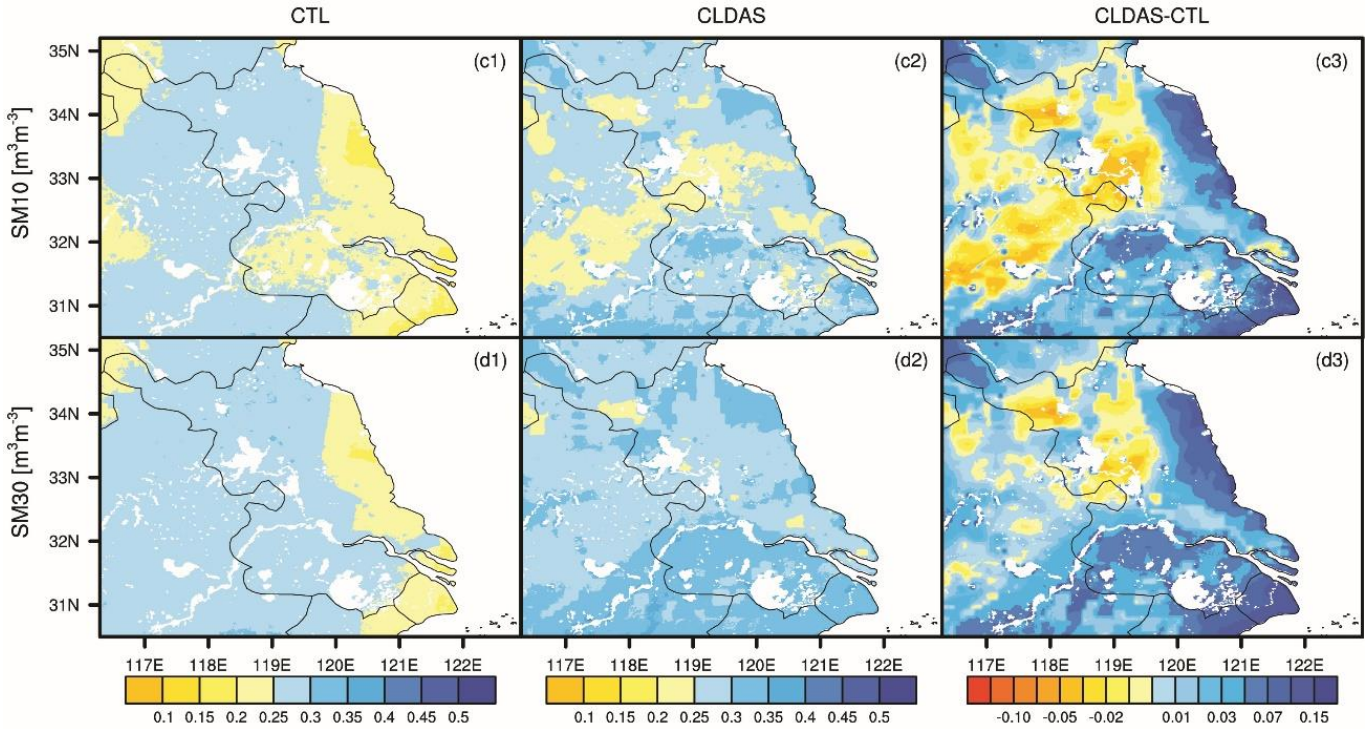


Figure 3. Spatial-distribution characteristics and relative differences over research period in EC. (**a1**,**a2**,**a3**) Albedo and relative difference between WRF and MODIS data; (**b1**,**b2**,**b3**) LAI and relative difference between WRF and MODIS data; (**c1**,**c2**,**c3**) 10 cm soil water and relative difference between WRF and CLDAS data (unit: m^3m^{-3}) and (**d1**,**d2**,**d3**) 30 cm soil water and relative difference between WRF and CLDAS data (unit: m^3m^{-3}).

Generally, it is remarkable that the MODIS albedo and LAI could accurately describe the spatial distribution characteristics comparing the default climatology albedo and LAI, which are more suitable for high-resolution simulations. Area-averaged CLDAS SM data were higher by 12.36% to 18.09% than those of the ERA SM.

3.2. Model Validation

To validate the performance of the developed modeling system, the simulation results of the WRF_CTL were compared with the observed Ta from the AWS network. Figures 4a and 5a show the spatial distribution of the observed Ta during the hot weather in EC, particularly mean Ta and Tamax. The large-area higher-observation Ta appeared south of Jiangsu province and the Shanghai, and the highest 5 day mean observation Ta reached 36.60 °C (Figure 4a). The WRF_CTL simulation could effectively capture the spatial distribution of Ta with a spatial correlation coefficient (SCC) of 0.77 compared with the observed Ta (Figure 4b). However, the WRF_CTL simulation systematically overestimated the Ta with a warming bias of 1.05 °C in most of the study area (Figure 4b,c).

The spatial distribution of observation Tamax had a similar pattern with that of observation Ta. The daily highest hourly observation Tamax of 41.10 °C appeared south of Jiangsu, and the 5 day mean observation Tamax is about 39.86 °C (Figure 5a). The WRF_CTL simulation could capture the spatial distribution of Tamax, and the SCC between observed Tamax and WRF_CTL Tamax is 0.67 (Figure 5b). The CTL simulation also overestimated the Tamax with a warming bias of 1.32 °C (Figure 5b,c). Comparing the simulated Ta by WRF_CTL, the SCC between simulated and observed Tamax was lower, but the warming bias was higher. Table 2 compares the statistical values of the observed and simulated 5-day mean Ta and Tamax in the study region.

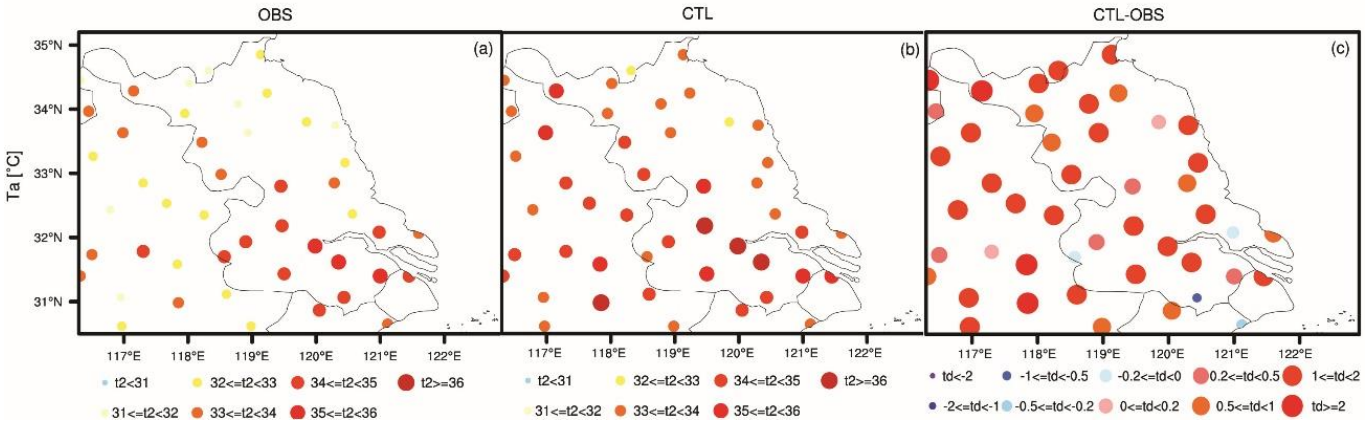


Figure 4. (**a**) Daily averaged observed air temperature, (**b**) simulated air temperature, and (**c**) their difference (unit: °C) over the research period in EC.

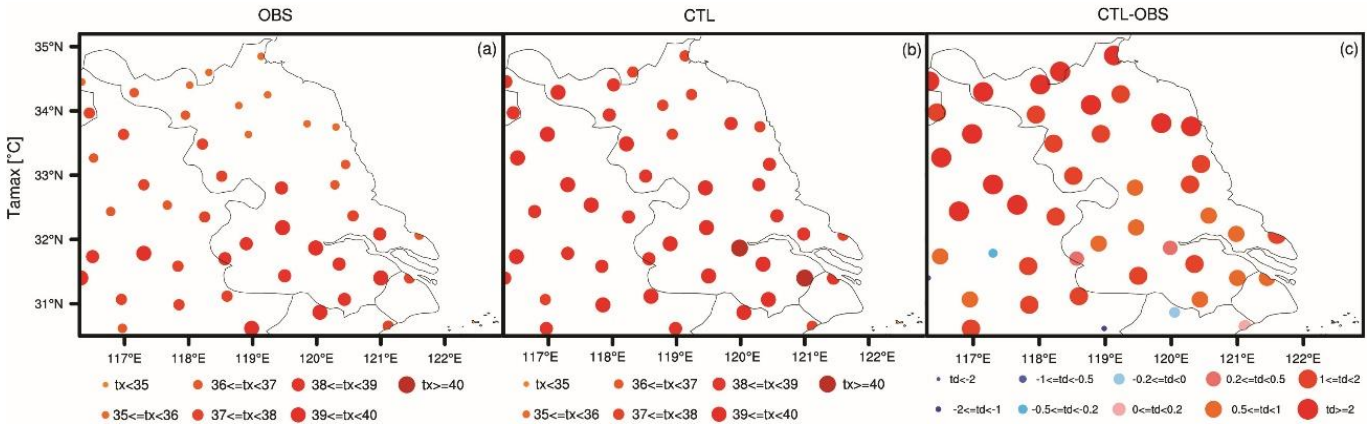


Figure 5. (**a**) Daily averaged observed maximal air temperature, (**b**) simulated maximal air temperature, and (**c**) their difference (unit: °C) over the research period in EC.

Table 2. Statistical values of observed and simulated 5-day mean Ta and Tamax in study region, °C.

	MEAN		STD		BIAS	RMSE	SCC
	OBS	CTL	OBS	CTL			
Ta	33.10	34.15	1.12	1.13	1.05	1.29	0.77
Tamax	37.32	38.64	1.42	1.12	1.32	1.69	0.67

OBS: observation, CTL: WRF_CTL experiment, MEAN: mean value, STD: standard deviation, BIAS: systematic bias, RMSE: root mean square error, SCC: spatial correlation coefficient.

3.3. Impact of LSCPs on Air Temperature

To investigate the impact of LSC on hot weather, results from control simulation WRF_CTL and sensitivity simulation WRF_CHAR were compared and analyzed. Figure 6 shows the simulated averaged Ta and the difference in the modeling period by WRF_CTL and WRF_CHAR simulations. WRF_CTL and WRF_CHAR presented similar Ta patterns, and the higher temperature regions mainly appeared to be cities, such as Nanjing, Wuxi, Zhenjiang, and Shanghai. However, WRF_CHAR obtained a higher Ta than WRF_CTL did, especially east of Jiangsu, with a minus difference of 2 °C. In most of the southern region of Jiangsu, a cold bias of 0.2–1.0 °C was found, but north of Jiangsu, a slight warming bias of 0.2–0.4 °C appeared. Generally, a 5 day area-averaged Ta by WRF_CHAR showed a slight cold bias of 0.38 °C compared with that in WRF_CTL.

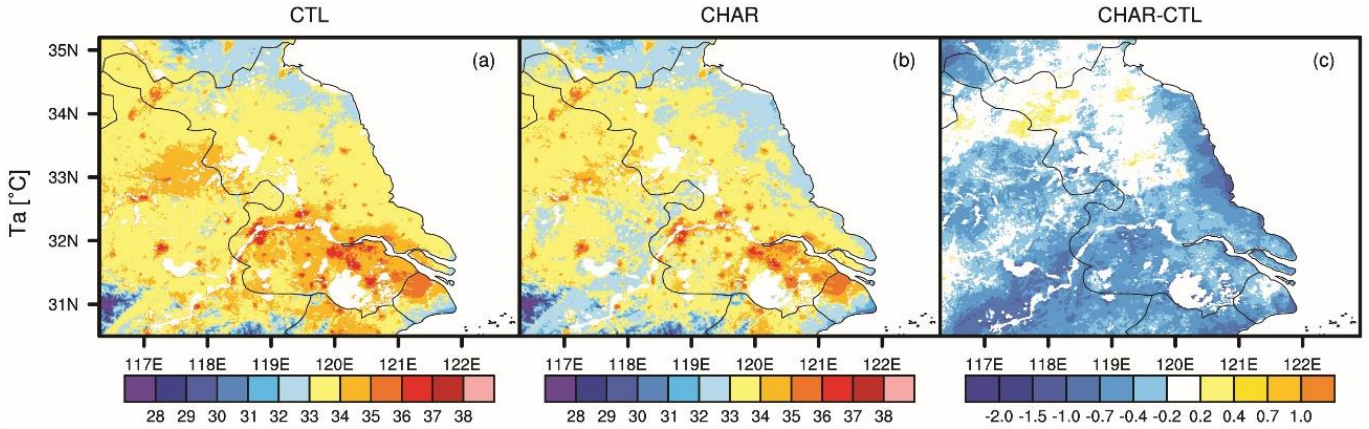


Figure 6. Spatial distribution of mean air temperature (unit: °C) for (**a**) CTL experiment, (**b**) CHAR experiment, and (**c**) their difference over the research period in EC.

The surface temperature (Ts) had a similar result with Ta from WRF_CTL and WRF_CHAR (figures not shown), but a cold bias of more than 3 °C appeared in the east side of Jiangsu, and a 5 day area-averaged Ts displayed a cold bias of 0.72 °C.

Figure 7a presents the hourly variations of area-averaged observed and simulated Ta and their differences in EC. Tamax was observed to occur at approximately 16:00 local standard time (LST) by observation, WRF_CTL and WRF_CHAR. WRF_CTL obtained a higher Ta than the observation did at almost the entire diurnal time period, the maximal warming bias was approximately 1.9 °C, and the averaged warming bias was 1.07 °C (Figure 7b). The Ta from WRF_CHAR was lower than that from WRF_CTL, with a maximal warming bias of 1.5 °C and an averaged warming bias of 0.71 °C, which was closer to the observed value and significantly reduced the warming bias. Statistical results showed that the WRF_CHAR slightly improved the simulated Ta with a value of 33.08%.

Figure 8 presents the spatial distribution of mean Tamax for WRF_CTL, WRF_CHAR, and their difference, which presented a similar result with that in Figure 6, and WRF_CHAR generally obtained a lower Tamax than WRF_CTL did, with an area-averaged difference of approximately 0.45 °C. Daily variations of area-averaged observed and simulated Tamax obviously showed that WRF_CHAR obtained a lower Tamax than WRF_CTL did, though still higher than that of the observation. Comparing the observations, WRF_CHAR reduced warming bias from 1.31 to 0.92 °C. That is to say, CHAR improved the simulated Tamax of 29.24% (Figure 9).

3.4. Impact of LSCPs on Surface Energy Balance

LSCs modulate the partition of total available energy at the land surface between sensible heat fluxes (SHs) and latent heat fluxes (LHs), determine temperature and moisture at the interface between soil or vegetation and the atmosphere, and then impact near-surface atmospheric conditions [14,24], further resulting in changes in air temperature [24].

Figure 10 displays the 5 day averaged surface energy-flux differences between WRF_CHAR and WRF_CTL in EC. As is shown in Figure 10a, large areas had a negative SH difference, which was very similar with the Ta differences (Figure 6c), with an area-averaged SH difference of -9.25 Wm^{-2}, especially east of Jiangsu, with a minimal SH difference of about -30 Wm^{-2}. LH differences presented the opposite pattern when comparing SH differences, which mainly showed positive values in most areas with an area average of 13.35 Wm^{-2}, and the maximal SH difference was more than 30 Wm^{-2}. Generally, net radiation flux (Rn) presented a positive difference with an area average of 3.57 Wm^{-2}, the positive Rn was mainly distributed in the southeastern region of the research area, and the negative difference appeared northwest of the research area. Soil heat flux (GH) showed a slight positive difference with an area average of 0.35 Wm^{-2}. In

the south of the research area, GH differences of 1–3 Wm^{-2} appeared, but in the north of the research area, there was a -1 to -3 Wm^{-2} GH difference.

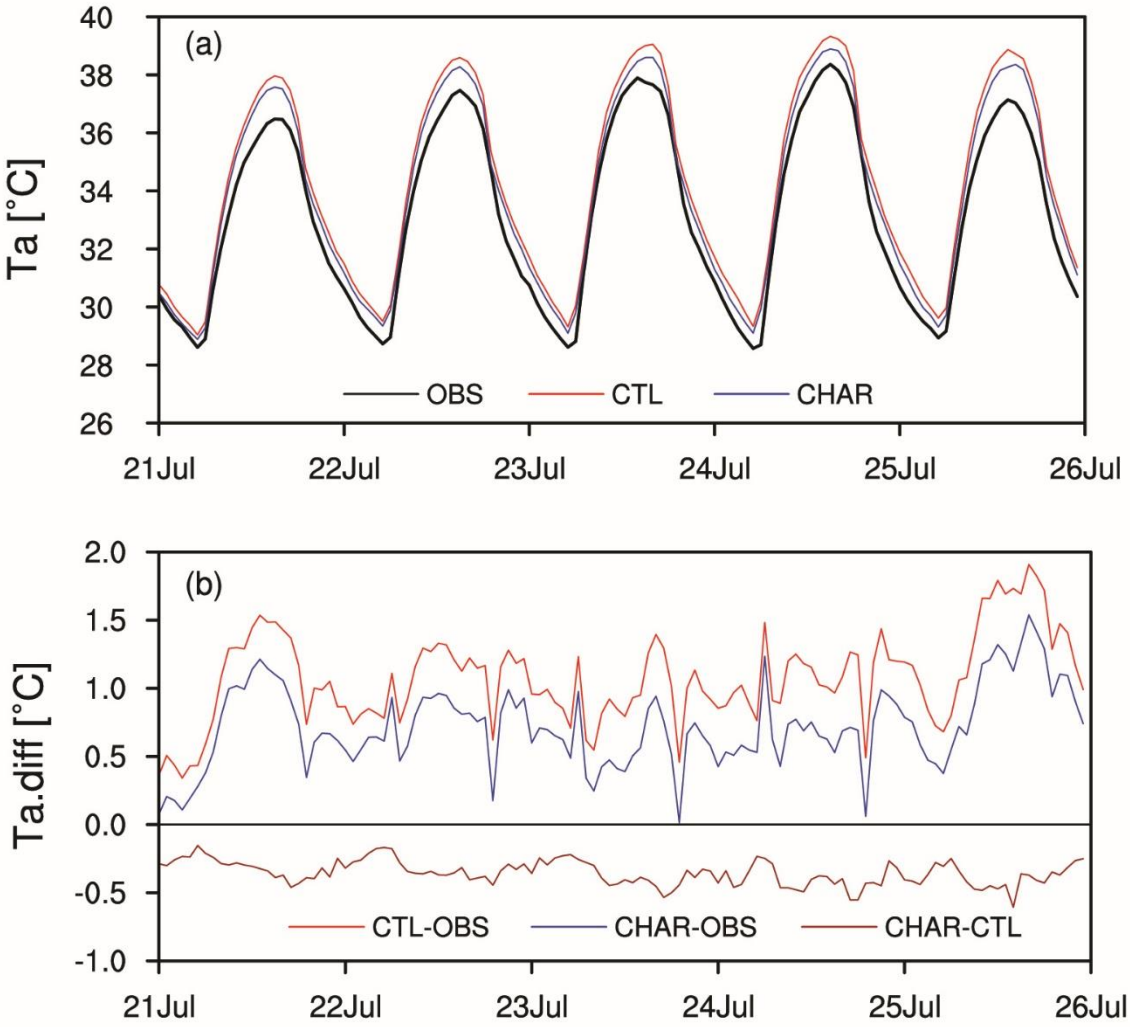


Figure 7. (**a**) Hourly variations of area-averaged observed and simulated air temperature, and (**b**) their difference (unit: °C) over the research period in EC.

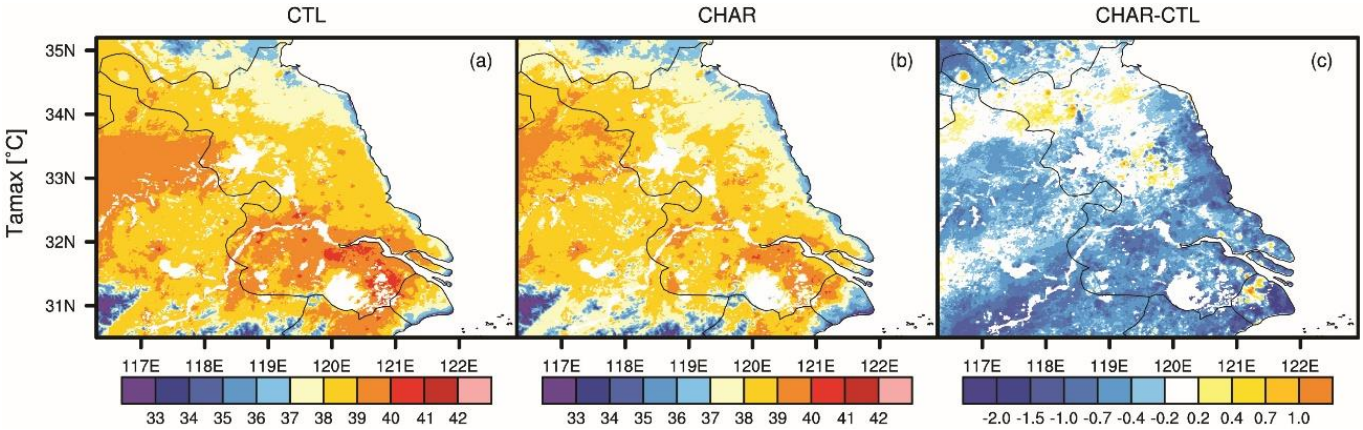


Figure 8. Spatial distribution of mean maximal air temperature (unit: °C) for (**a**) CTL experiment, (**b**) CHAR experiment, and (**c**) their difference over the research period in EC.

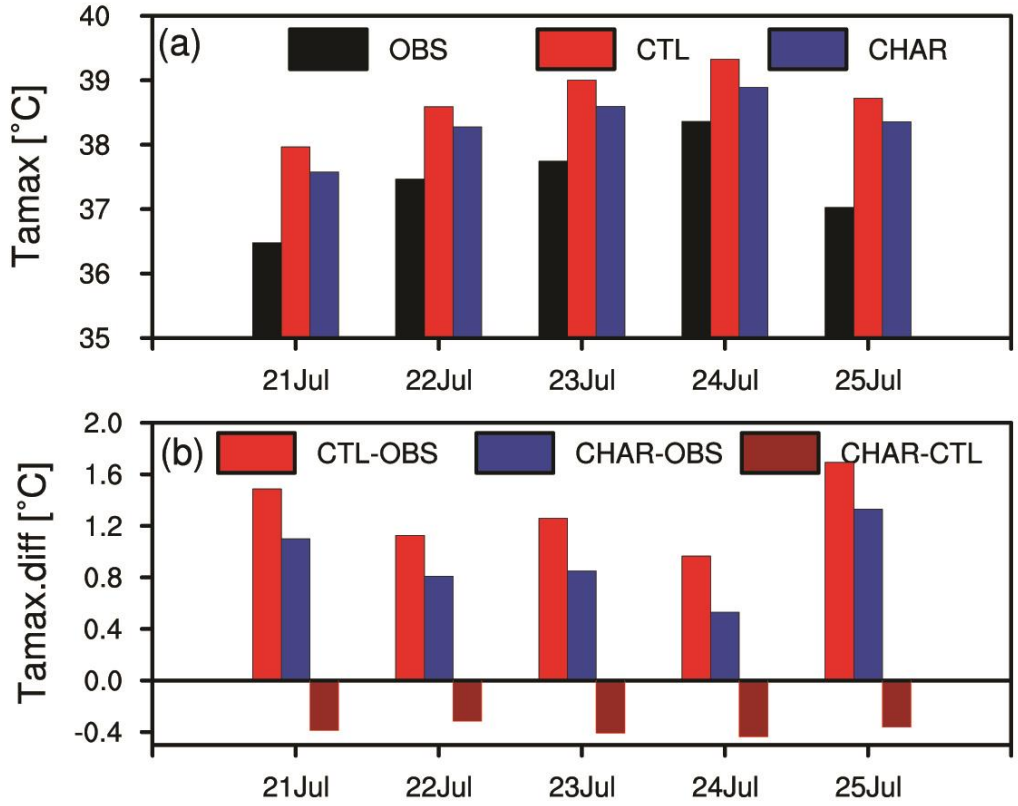


Figure 9. (**a**) Daily variations of area-averaged observed and simulated maximal air temperature, and (**b**) their difference (unit: °C) over the research period in EC.

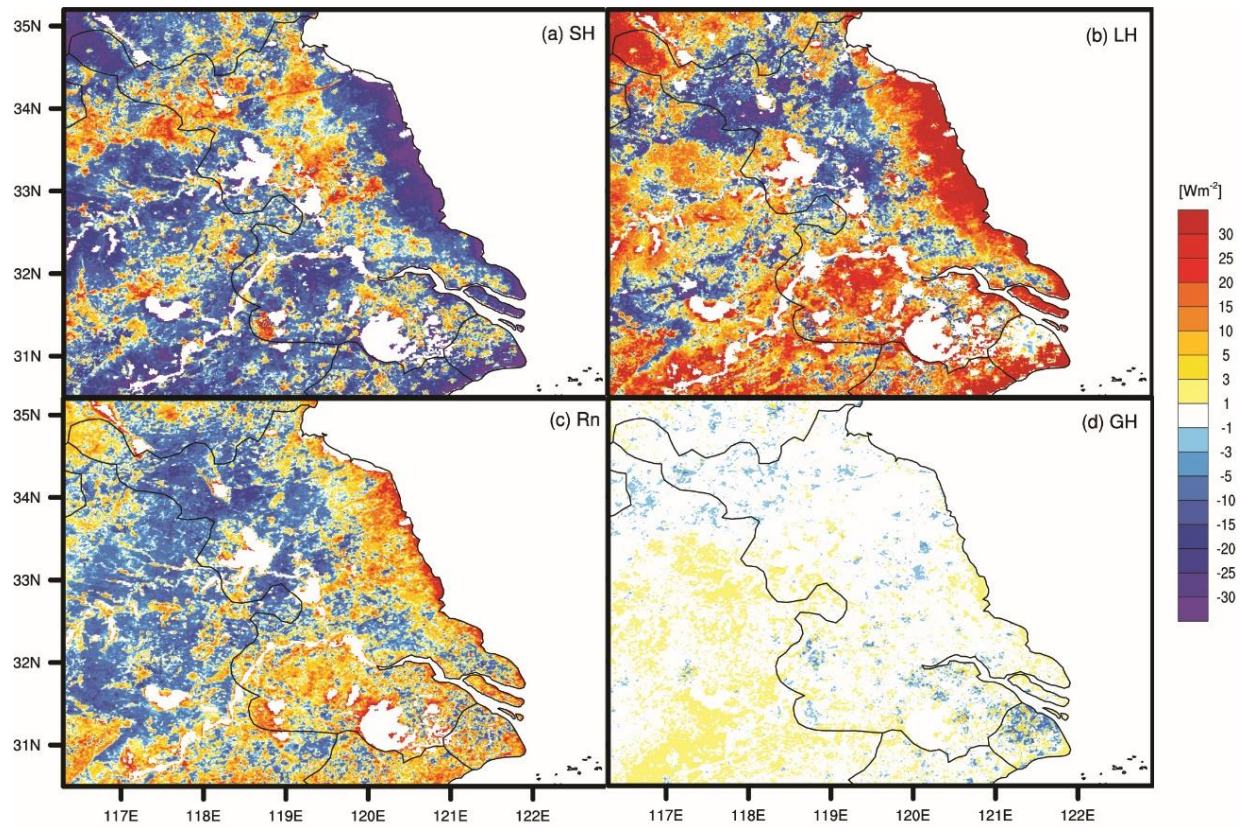


Figure 10. Spatial distribution of mean surface energy differences (unit: Wm^{-2}) between CTL and CHAR experiments over the research period in EC: (**a**) sensible heat flux, (**b**) latent heat flux, (**c**) net radiation flux, and (**d**) ground heat flux.

The temporal variation of area-averaged surface energy-flux differences showed minimal SH differences, and maximal LH, Rn, and GH differences appearing in the day time, especially occurring at approximately 16:00 local standard time (LST), which corresponds to Ta variation (Figure 7a). Obviously, the change in LSCP albedo, LAI, and soil moisture affected energy allocation. Albedo, LAI, and soil moisture affected the energy balance through shortwave radiation, canopy resistance, and surface evaporation, respectively. On the basis of Monin–Obukhov similarity theory, the surface energy flux established the relationship between the surface layer profiles of temperature, humidity, and wind speed through atmospheric turbulence in the atmosphere boundary layer, from which air temperature is changed.

3.5. Impact Comparison of Different LSCPs on Air Temperature

In this research, two LSCP types (albedo and LAI) and one type of land soil variation (SM) were integrated into the WRF model to research the impact of LSC on hot weather in EC. Sensitivity simulation WRF_CHAR, in which the LSCPs were updated, improved Ta and Tamax. However, it is still a problem that different LSCPs have a different effect or contribution on higher temperature, and which LSCP is the main affecting factor needs to be established.

Figure 11 shows the scatter diagram of spatial-grid cell-based albedo, LAI, and SM of 10 cm differences, and the corresponding Ta differences of simulations from WRF_CHAR and WRF_CTL. Albedo and Ta differences had positive correlation with a value of 0.02 (Figure 11a). LAI and Ta differences had negative correlation with a value of −0.37 (Figure 11b). Moreover, SM10 and Ta differences obtained negative correlation of −0.68, which was the largest absolute value of the correlation coefficient (Figure 11c).

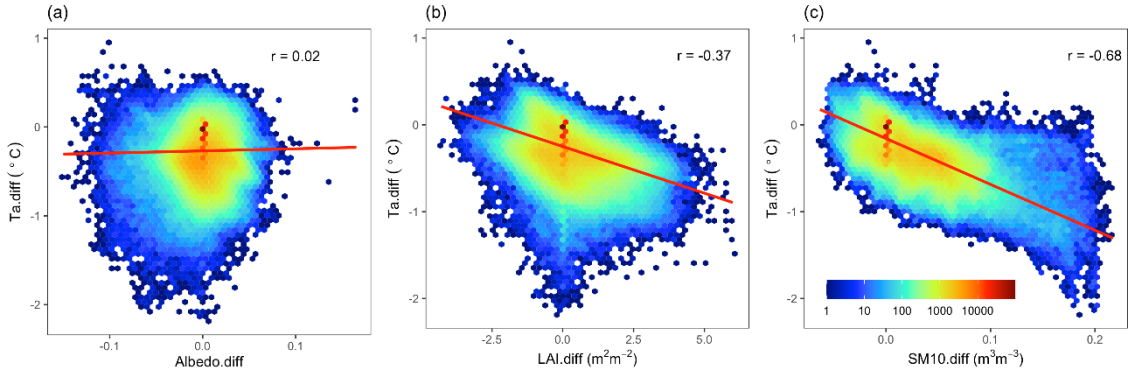


Figure 11. Density scatter diagram of (**a**) albedo difference, (**b**) LAI difference, and (**c**) 10 cm soil moisture difference, and corresponding air-temperature difference.

The spatial distribution of the passed confidence-test correlation coefficient between Ta, albedo, LAI, and SM10 differences further supports the results of Figure 11 (Figure 12). The correlation coefficient between Ta and SM10 differences presented patchy large-area negative values, and the other correlation coefficients mainly presented point spatial distribution.

To further confirm the result, excluding WRF_CTL and WRF_CHAR, four more numerical simulations were performed: WRF_ALB (just updated the albedo), WRF_LAI (just updated the LAI), WRF_ALL (updated the albedo and LAI), and WRF_CLDAS (just updated the four layers' SM). The hourly variation of area-averaged observed Ta and simulated Ta from six numerical simulations and their differences are displayed in Figure 13. Comparing the five other simulations, area-averaged Ta from WRF_CLDAS were closer to those from WRF_CHAR, which together integrated the albedo, LAI and SM, especially in the daytime, which means that SM had the maximal contribution to improving the warming Ta bias. The albedo and LAI just resulted in a slight change in area-averaged Ta, and the effect of albedo and LAI on Ta and Tamax is mainly reflected in spatial distribution characteristics (figures not shown).

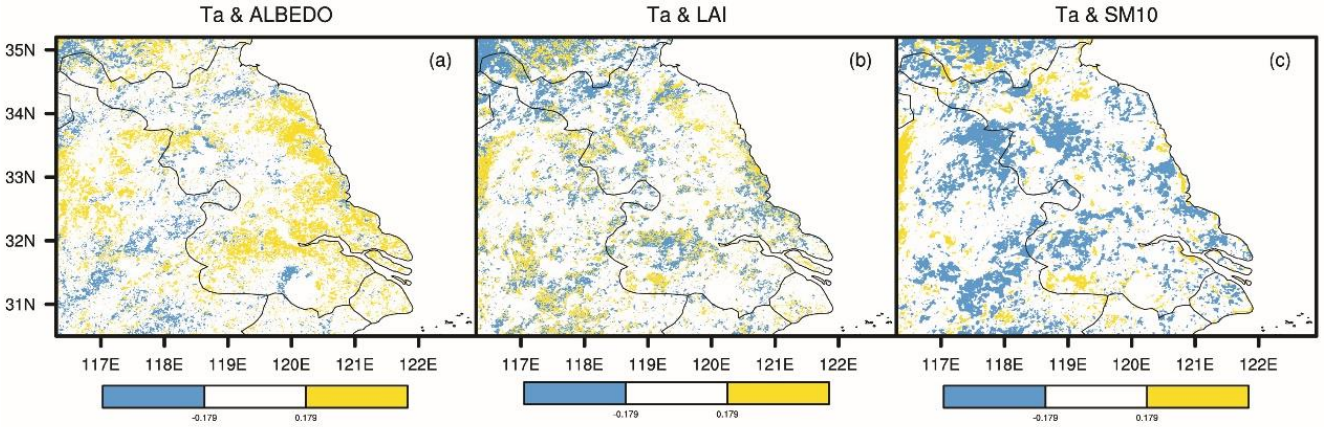


Figure 12. Spatial distribution of correlation coefficient (r) between (**a**) air-temperature and albedo difference, (**b**) LAI difference, and (**c**) 10 cm soil water difference over the research period in EC.

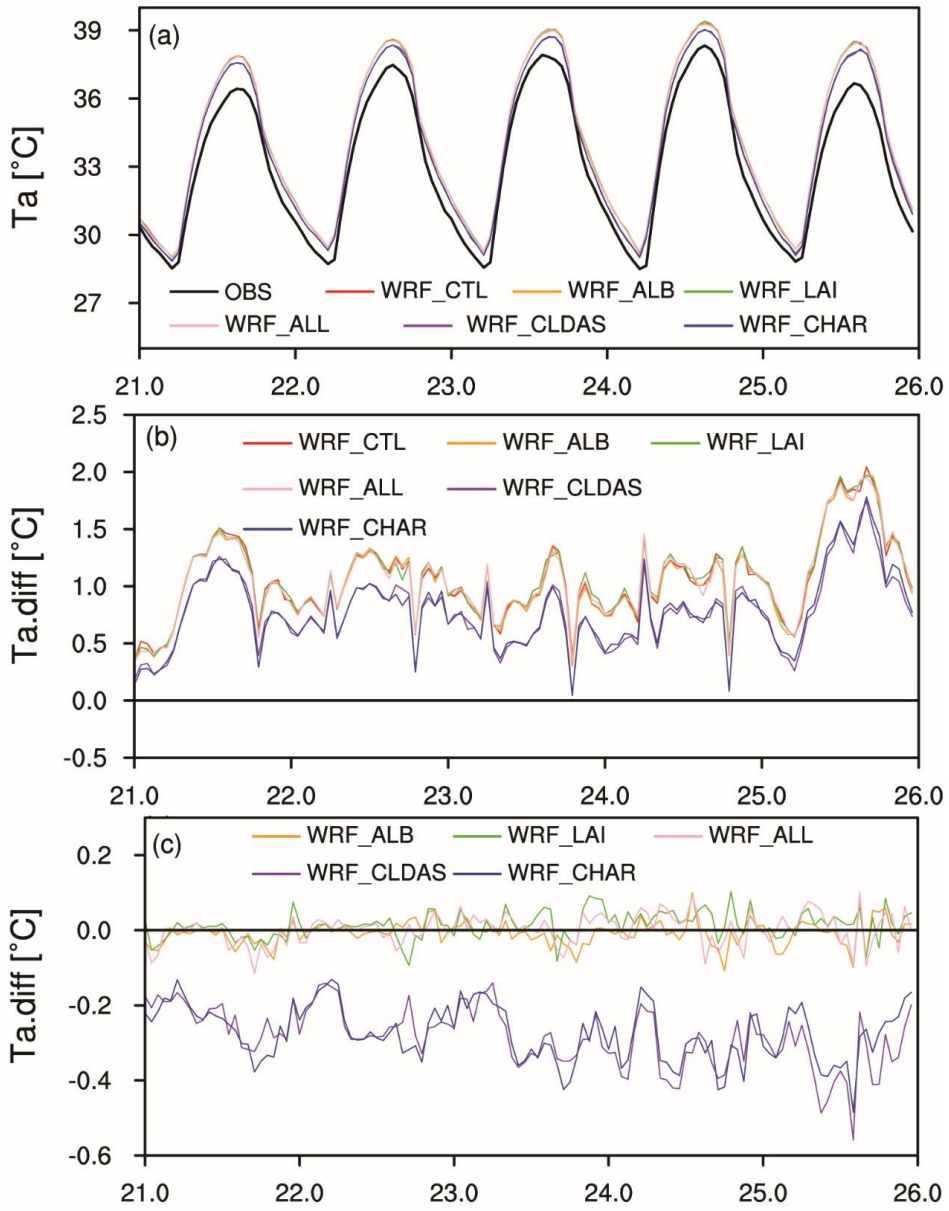


Figure 13. (**a**) Hourly variations of area-averaged observed and simulated air temperature and (**b**,**c**) their difference (unit: °C) over the research period by the supplementary simulation in EC.

We integrated remote-sensing LSCP albedo and LAI and assimilation SM into the WRF model, and air temperature was improved. However, there are still remaining biases between the simulated and observed air temperature. This is probably due to uncertainties in the WRF model, atmospheric forcing data, and LSCP albedo, LAI, and assimilation SM data. In the past few years, numerical forecasting models have been improved, but some processes are still poorly simulated [13]. Additionally, atmospheric forcing data from different general atmospheric-circulation models or general atmosphere–ocean circulation models still have differences, which can also induce inaccurate simulations [51]. Satellite-based LSCP albedo and LAI and assimilation SM data are better than before, but different remote-sensing albedo and LAI and assimilation SM still have differences and can cause air temperature bias [52,53].

4. Conclusions

In this study, to investigate the impact of LSCP albedo and LAI and SM on hot weather that occurred in EC on 21–25 July 2017, a control simulation with the WRF model default LSCPs, and a series of sensitivity simulations with the satellite- and assimilation-based data were performed. The simulated Ta and Tamax were compared with the station observations. Then, we compared and analyzed the results of the control, and performed a series of sensitivity simulations. The conclusions can be summarized as follows:

1. MODIS albedo and LAI, and CLDAS SM can better describe spatial distribution characteristics, and match fine weather forecasts and high-resolution simulations than the default climatology albedo and LAI can. The area-averaged accuracy of CLDAS SM data was higher by 12.36% to 18.09% than that of the ERA SM.
2. The control simulation WRF_CTL could capture the spatial distribution of Ta and Tamax, but overestimated the Ta and Tamax with a warming bias of 1.05 and 1.32 °C, respectively. Sensitivity simulation WRF_CHAR improved the simulated Ta and Tamax by 33.08% and 29.24%, respectively.
3. Comparing the WRF_CTL simulation, the WRF_CHAR simulation presented an area-averaged SH difference of -9.25 Wm^{-2}, LH difference of -9.25 Wm^{-2}, and Rn difference of 3.57 Wm^{-2}. The updated albedo, LAI, and SM changed the partition of surface energy and then resulted in a change of Ta and Tamax.
4. Soil moisture is the main factor to improve warming bias in hot weather in EC based on the scatter diagram and the spatial correlation coefficient of albedo, LAI, and SM10 and Ta.

Author Contributions: S.L. (Suosuo Li) and Y.L. designed and performed the numerical simulations, and processed the data; Y.L. and Y.P. helped to analyze the data and plotted the figures; Z.L. helped to setup the WRF model and download the forcing fields; S.L. (Suosuo Li) wrote the paper with the help and suggestions of Y.L. and S.L. (Shihua Lyu). All authors have read and agreed to the published version of the manuscript.

Funding: This work was jointly supported by the National Key R&D Program of China (2017YFC1502101), the National Natural Science Foundation of China (41805079, 42075090, 41805073, and 41930759), and the Science and Technology Plan of Gansu Province, China (20JR10RA070).

Acknowledgments: MODIS albedo and LAI data from Oak Ridge National Laboratory (ORNL) Distributed Active Archive Center (DAAC) (https://daac.ornl.gov/LAND_VAL/guides/MODIS_Web_Service_C6.html, accessed on 7 February 2020), assimilation soil moisture data from China Meteorological Administration (CMA) Land Data Assimilation System (CLDAS) (http://data.cma.cn/dataService/cdcindex/datacode/NAFP_CLDAS2.0_RT.html, accessed on 11 February 2020) and 2 m air temperature datasets from the Climatic Data Center, the National Meteorological Information Center, CMA (http://data.cma.cn/site/index.html, accessed on 11 February 2020). We also thank the European Centre for Medium-Range Weather Forecasts for providing ERA-Interim data as the forcing fields.

Conflicts of Interest: The authors declare no conflict of interest.

References

1. Bindi, M.; Brown, S.; Camilloni, I.; Diedhiou, A.; Djalante, R.; Ebi, K.; Engelbrecht, F.; Guiot, J.; Hijioka, Y.; Mehrotra, S. *Impacts of 1.5 °C of Global Warming on Natural and Human Systems*; IPCC: Geneva, Switzerland, 2018.
2. Shi, J.; Ding, Y.H.; Cui, L.L. Climatic characteristics of extreme maximum temperature in East China and its causes. *Chin. J. Atmos. Sci.* **2009**, *33*, 347–358.
3. Lin, X.; Guan, Z.Y. Temporal spatial characters and interannual variations of summer high temperature in East China. *J. Nanjing Inst. Meteorol.* **2008**, *31*, 1–9.
4. Zhang, J.; Wu, L. Land-atmosphere coupling amplifies hot extremes over China. *Chin. Sci. Bull.* **2011**, *56*, 3328–3332. [CrossRef]
5. Vahmani, P.; Ban-Weiss, G.A. Impact of remotely sensed albedo and vegetation fraction on simulation of urban climate in WRF-urban canopy model: A case study of the urban heat island in Los Angeles. *J. Geophys. Res. Atmos.* **2016**, *121*, 1511–1531. [CrossRef]
6. Xiao, H.; Liu, Y.; Li, L.; Yu, Z.; Zhang, X. Spatial variability of local rural landscape change under rapid urbanization in Eastern China. *ISPRS Int. J. Geo-Inf.* **2018**, *7*, 231. [CrossRef]
7. Zhou, D.; Bonafoni, S.; Zhang, L.; Wang, R. Remote sensing of the urban heat island effect in a highly populated urban agglomeration area in East China. *Sci. Total Environ.* **2018**, *628–629*, 415–429. [CrossRef]
8. Chen, F.; Yang, X.; Zhu, W. WRF simulations of urban heat island under hot-weather synoptic conditions: The case study of Hangzhou City, China. *Atmos. Res.* **2014**, *138*, 364–377. [CrossRef]
9. Zeng, X.-M.; Wang, B.; Zhang, Y.; Song, S.; Huang, X.; Zheng, Y.; Chen, C.; Wang, G. Sensitivity of high-temperature weather to initial soil moisture: A case study using the WRF model. *Atmos. Chem. Phys. Discuss.* **2014**, *14*, 9623–9639. [CrossRef]
10. Gao, Z.; Zhu, J.; Guo, Y.; Luo, N.; Fu, Y.; Wang, T. Impact of land surface processes on a record-breaking rainfall event on 6–7 May 2017, in Guangzhou, China. *J. Geophys. Res. Atmos.* **2021**, *126*, e2020JD032997. [CrossRef]
11. Council, N.R.; Committee, C.R. *GOALS (Global Ocean-Atmosphere-Land System) for Predicting Seasonal-to-Interannual Climate: A Program of Observation, Modeling, and Analysis*; National Academies Press: Washington, DC, USA, 1994.
12. Dirmeyer, P.A. The terrestrial segment of soil moisture-climate coupling. *Geophys. Res. Lett.* **2011**, *38*. [CrossRef]
13. Meng, X.; Lyu, S.; Zhang, T.; Zhao, L.; Li, Z.; Han, B.; Li, S.; Ma, D.; Chen, H.; Ao, Y.; et al. Simulated cold bias being improved by using MODIS time-varying albedo in the Tibetan Plateau in WRF model. *Environ. Res. Lett.* **2018**, *13*, 044028. [CrossRef]
14. Gao, Y.; Chen, F.; Barlage, M.; Liu, W.; Cheng, G.; Li, X.; Yu, Y.; Ran, Y.; Li, H.; Peng, H.; et al. Enhancement of land surface information and its impact on atmospheric modeling in the Heihe River Basin, northwest China. *J. Geophys. Res. Space Phys.* **2008**, *113*. [CrossRef]
15. Boussetta, S.; Balsamo, G.; Beljaars, A.; Kral, T.; Jarlan, L. Impact of a satellite-derived leaf area index monthly climatology in a global numerical weather prediction model. *Int. J. Remote Sens.* **2012**, *34*, 3520–3542. [CrossRef]
16. Feddema, J.J.; Oleson, K.W.; Bonan, G.B.; Mearns, L.O.; Buja, L.E.; Meehl, G.A.; Washington, W.M. The importance of land-cover change in simulating future climates. *Science* **2005**, *310*, 1674–1678. [CrossRef]
17. Knote, C.; Bonafé, G.; Di Giuseppe, F. Leaf area index specification for use in mesoscale weather prediction systems. *Mon. Weather Rev.* **2009**, *137*, 3535–3550. [CrossRef]
18. Kumar, A.; Chen, F.; Barlage, M.; Ek, M.B.; Niyogi, D. Assessing impacts of integrating MODIS vegetation data in the weather research and forecasting (WRF) model coupled to two different canopy-resistance approaches. *J. Appl. Meteorol. Clim.* **2014**, *53*, 1362–1380. [CrossRef]
19. Boussetta, S.; Balsamo, G.; Dutra, E.; Beljaars, A.; Albergel, C. *Analysis of Surface Albedo and Leaf Area Index from Satellite Observations and Their Impact on Numerical Weather Prediction*; European Centre for Medium-Range Weather Forecasts: Reading, UK, 2014.
20. Li, S.; Gao, Y.; Lyu, S.; Liu, Y.; Pan, Y. Response of surface air temperature to the change of leaf area index in the source region of the Yellow River by the WRF model. *Theor. Appl. Clim.* **2019**, *138*, 1755–1765. [CrossRef]
21. Yan, D.; Liu, T.; Dong, W.; Liao, X.; Luo, S.; Wu, K.; Zhu, X.; Zheng, Z.; Wen, X. Integrating remote sensing data with WRF model for improved 2-m temperature and humidity simulations in China. *Dyn. Atmos. Ocean.* **2019**, *89*, 101127. [CrossRef]
22. Zhang, M.; Luo, G.; De Maeyer, P.; Cai, P.; Kurban, A. Improved atmospheric modelling of the oasis-desert system in Central Asia using WRF with actual satellite products. *Remote Sens.* **2017**, *9*, 1273. [CrossRef]
23. Zhang, H.; Liu, J.; Li, H.; Meng, X.; Ablikim, A. The impacts of soil moisture initialization on the forecasts of weather research and forecasting model: A case study in Xinjiang, China. *Water* **2020**, *12*, 1892. [CrossRef]
24. Lin, T.-S.; Cheng, F.-Y. Impact of soil moisture initialization and soil texture on simulated land—Atmosphere interaction in Taiwan. *J. Hydrometeorol.* **2016**, *17*, 1337–1355. [CrossRef]
25. Meng, L.; Shen, Y. On the relationship of soil moisture and extreme temperatures in East China. *Earth Interact.* **2014**, *18*, 1–20. [CrossRef]
26. Seneviratne, S.I.; Corti, T.; Davin, E.; Hirschi, M.; Jaeger, E.B.; Lehner, I.; Orlowsky, B.; Teuling, A. Investigating soil moisture-climate interactions in a changing climate: A review. *Earth Sci. Rev.* **2010**, *99*, 125–161. [CrossRef]
27. Zhang, J.; Wu, L.; Dong, W. Land-atmosphere coupling and summer climate variability over East Asia. *J. Geophys. Res. Space Phys.* **2011**, *116*. [CrossRef]
28. Koster, R.D.; Sud, Y.; Guo, Z.; Dirmeyer, P.A.; Bonan, G.; Oleson, K.W.; Chan, E.; Verseghy, D.; Cox, P.; Davies, H. GLACE: The global land-atmosphere coupling experiment. Part I: Overview. *J. Hydrometeorol.* **2006**, *7*, 590–610. [CrossRef]

29. Hong, S.; Lakshmi, V.; Small, E.; Chen, F.; Tewari, M.; Manning, K.W. Effects of vegetation and soil moisture on the simulated land surface processes from the coupled WRF/Noah model. *J. Geophys. Res. Space Phys.* **2009**, *114*. [CrossRef]
30. Zhang, J.; Dong, W. Soil moisture influence on summertime surface air temperature over East Asia. *Theor. Appl. Clim.* **2009**, *100*, 221–226. [CrossRef]
31. Dy, C.Y.; Fung, J.C.H. Updated global soil map for the weather research and forecasting model and soil moisture initialization for the Noah land surface model. *J. Geophys. Res. Atmos.* **2016**, *121*, 8777–8800. [CrossRef]
32. Yao, T.; Xue, Y.; Chen, D.; Chen, F.; Thompson, L.; Cui, P.; Koike, T.; Lau, W.K.-M.; Lettenmaier, D.; Mosbrugger, V.; et al. Recent third pole's rapid warming accompanies cryospheric melt and water cycle intensification and interactions between monsoon and environment: Multidisciplinary approach with observations, modeling, and analysis. *Bull. Am. Meteorol. Soc.* **2019**, *100*, 423–444. [CrossRef]
33. Zhou, X.; Yang, K.; Ouyang, L.; Wang, Y.; Jiang, Y.; Li, X.; Chen, D.; Prein, A. Added value of kilometer-scale modeling over the third pole region: A CORDEX-CPTP pilot study. *Clim. Dyn.* **2021**, 1–15. [CrossRef]
34. EnTao, Y. A warmer, wetter and less windy China in the twenty-first century as projected by a nested high-resolution simulation using the weather research and forecasting (WRF) model. *Asia-Pac. J. Atmos. Sci.* **2018**, *55*, 53–74. [CrossRef]
35. Rasmussen, R.; Liu, C.; Ikeda, K.; Gochis, D.; Yates, D.; Chen, F.; Tewari, M.; Barlage, M.; Dudhia, J.; Yu, W.; et al. High-resolution coupled climate runoff simulations of seasonal snowfall over Colorado: A process study of current and warmer climate. *J. Clim.* **2011**, *24*, 3015–3048. [CrossRef]
36. Wanders, N.; Van Vliet, M.T.H.; Wada, Y.; Bierkens, M.F.P.; Van Beek, L.P.H. High-resolution global water temperature modeling. *Water Resour. Res.* **2019**, *55*, 2760–2778. [CrossRef]
37. Lin, L.-F.; Ebtehaj, A.M.; Flores, A.N.; Bastola, S.; Bras, R.L. Combined assimilation of satellite precipitation and soil moisture: A case study using TRMM and SMOS. *Data. Mon. Weather Rev.* **2017**, *145*, 4997–5014. [CrossRef]
38. Lin, L.-F.; Pu, Z. Examining the impact of SMAP soil moisture retrievals on short-range weather prediction under weakly and strongly coupled data assimilation with WRF-Noah. *Mon. Weather Rev.* **2019**, *147*, 4345–4366. [CrossRef]
39. Findell, K.L.; Eltahir, E.A. Atmospheric controls on soil moisture-boundary layer interactions. Part I: Framework development. *J. Hydrometeorol.* **2003**, *4*, 552–569. [CrossRef]
40. Wang, G.; Ye, D.; Zhang, Y.; Huang, D.; Hou, W. Characteristics and abnormal atmospheric circulation of regional high temperature process in 2017 over China. *Adv. Clim. Chang. Res.* **2018**, *14*, 341.
41. Csiszar, I.; Gutman, G. Mapping global land surface albedo from NOAA AVHRR. *J. Geophys. Res. Space Phys.* **1999**, *104*, 6215–6228. [CrossRef]
42. Viterbo, P.; Beljaars, A.C.M. An improved land surface parameterization scheme in the ECMWF model and its validation. *J. Clim.* **1995**, *8*, 2716–2748. [CrossRef]
43. Vannan, S.K.S.; Cook, R.B.; Holladay, S.K.; Olsen, L.M.; Dadi, U.; Wilson, B.E. A web-based subsetting service for regional scale MODIS land products. *IEEE J. Sel. Top. Appl. Earth Obs. Remote. Sens.* **2009**, *2*, 319–328. [CrossRef]
44. Vannan, S.K.S.; Cook, R.B.; Pan, J.Y.; Wilson, B.E. A SOAP web service for accessing MODIS land product subsets. *Earth Sci. Inform.* **2011**, *4*, 97–106. [CrossRef]
45. Lo, J.C.F.; Yang, Z.L.; Pielke Sr, R.A. Assessment of three dynamical climate downscaling methods using the Weather Research and Forecasting (WRF) model. *J. Geophys. Res. Atmos.* **2008**, *113*. [CrossRef]
46. Chen, F.; Kusaka, H.; Bornstein, R.; Ching, J.; Grimmond, C.; Grossman-Clarke, S.; Loridan, T.; Manning, K.W.; Martilli, A.; Miao, S. The integrated WRF/urban modelling system: Development, evaluation, and applications to urban environmental problems. *Int. J. Climatol.* **2011**, *31*, 273–288. [CrossRef]
47. Chew, L.W.; Liu, X.; Li, X.-X.; Norford, L.K. Interaction between heat wave and urban heat island: A case study in a tropical coastal city, Singapore. *Atmos. Res.* **2020**, *247*, 105134. [CrossRef]
48. Hwang, M.-K.; Bang, J.-H.; Kim, S.; Kim, Y.-K.; Oh, I. Estimation of thermal comfort felt by human exposed to extreme heat wave in a complex urban area using a WRF-MENEX model. *Int. J. Biometeorol.* **2019**, *63*, 927–938. [CrossRef] [PubMed]
49. Morini, E.; Touchaei, A.G.; Castellani, B.; Rossi, F.; Cotana, F. The impact of Albedo increase to mitigate the urban heat island in Terni (Italy) using the WRF model. *Sustainability* **2016**, *8*, 999. [CrossRef]
50. Ramamurthy, P.; Li, D.; Bou-Zeid, E. High-resolution simulation of heatwave events in New York City. *Theor. Appl. Clim.* **2015**, *128*, 89–102. [CrossRef]
51. Wu, W.; Lynch, A.H.; Rivers, A. Estimating the uncertainty in a regional climate model related to initial and lateral boundary conditions. *J. Clim.* **2005**, *18*, 917–933. [CrossRef]
52. Tian, Y.; Woodcock, C.; Wang, Y.; Privette, J.L.; Shabanov, N.V.; Zhou, L.; Zhang, Y.; Buermann, W.; Dong, J.; Veikkanen, B.; et al. Multiscale analysis and validation of the MODIS LAI product: I. Uncertainty assessment. *Remote Sens. Environ.* **2002**, *83*, 414–430. [CrossRef]
53. Maggioni, V.; Houser, P.R. Soil moisture data assimilation. In *Data Assimilation for Atmospheric, Oceanic and Hydrologic Applications*; Springer: Berlin/Heidelberg, Germany, 2017; pp. 195–217.